Journal of Alloys and Compounds 994 (2024) 174693

Contents lists available at ScienceDirect

Journal of Alloys and Compounds

journal homepage: www.elsevier.com/locate/jalcom

Electrocatalytic reduction of CO_2 by Co-Cu metastable alloy nanoparticles derived from MOFs

Chi Song [a,b], Xiao Wang [a], Guanqing Song [a,b], Gansheng Shi [a], Yan Wang [a], Jiajun Yu [a,b], Xiaofeng Xie [a], Jing Sun [a,*]

[a] *State Key Lab of High Performance Ceramics and Superfine Microstructure, Shanghai Institute of Ceramics, Chinese Academy of Sciences, 1295 Dingxi Road, Shanghai 200050, China*
[b] *University of Chinese Academy of Sciences, 19 (A) Yuquan Road, Beijing 100049, China*

ARTICLE INFO

Keywords:
CO_2 electrocatalytic reduction
Syngas preparation
CoCu alloy
In-situ synthesis
DFT methods
Catalytic mechanism

ABSTRACT

The construction of non-noble metal electrodes for the catalytic reduction of CO_2 has drawn much attention in recent years. Herein, a facile CoCu@C composite catalyst was synthesized by simply carbonizing CoCu-MOFs, a bimetal MOFs fabricated by integrating Cu^{2+} ions into the synthesis of ZIF-67. Co-Cu alloy nanoparticles were closely embedded in porous carbon skeleton. Notably, the optimal Co_1Cu_3@C sample exhibited a total catalytic current of 29.8 $mA \cdot cm^{-2}$ at −0.7 V vs RHE, which was 2.56 times of the Co@C catalyst derived from original ZIF-67. Besides, the Co_1Cu_3@C sample achieved targeted $CO:H_2$ ratios in the CO_2 reduction reactions, covering approximately 1:1.7–1:4, meeting well with industrial needs. Density Functional Theory (DFT) calculations unveiled an electron migration from Co to Cu within the alloy, indicating the promoted transfer of electrons. Co atoms in Co-Cu alloy was found as the predominant active sites for the reduction of CO_2. The study provided a economical CO_2 reduction electrocatalyst with cheap feedstock, low operating voltage and specific ratio of syngas. Additionally, this work significantly advances our understanding of Co-Cu alloy electrocatalysts, providing crucial insights for the ongoing evolution of electrocatalyst research in material preparation and theoretical calculations.

1. Introduction

Rising concentration of carbon dioxide (CO_2) have led to global temperature rise and triggered worldwide attention. In response to these pressing concerns, technologies for carbon neutrality and CO_2 reduction show great practical significance. CO_2 electrocatalytic reduction, which can directly convert CO_2 into valuable chemical materials such as CO, CH_4 and H_2 under mild conditions, has been the focus in the domain of recent scientific researches [1–3].

The common products in CO_2 electrocatalytic reduction process include CO, methanol and formic acid, in conjunction with synchronous generation of H_2. However, it remains a challenge to collect liquid-phase products such as methanol and formic acid from electrolyte solution due to their low concentration. The cost of collection greatly limits the wider application of CO_2 electrocatalysis. On the comparison, the cost of gas-phase product separation is much lower, which made electrocatalytic reduction for "syngas" —a specific proportion of CO and hydrogens a promising means for practical applications [4]. The syngas with specific ratios such as $CO:H_2=1:1$, 1:2, and 1:3 are significant raw materials for the production of formaldehyde, methanol, methane and other industrial products [5]. Thus the reduction of CO_2 to CO and H_2 with appropriate ratio is desirable for reducing the collection cost and enhancing its applicability [6–8].

As competitive processes, modulating the rates of H_2 evolution and CO_2 reduction was found as the key to produce syngas with appropriate CO / H_2 ratio. Evidences exhibited a profound relationship between the catalyst adsorption energy and the competitive catalytic behavior [9,10]. Therefore, catalysts containing noble metals with most suitable adsorption energy for both H^+ and CO_2 were among the most promising candidates for the electrocatalytic reduction of CO_2 to syngas. However, the high cost and complex synthesis methods of noble metal nano-particles imposed limitations on their broader practical applications [11,12].

Electrocatalysts based on the non-precious metals such as thallium, lead, bismuth, indium, and cadmium, have also shown potential in CO_2 reduction. However, their relatively weak adsorption energy for H^+

---

* Corresponding author.
E-mail address: jingsun@mail.sic.ac.cn (J. Sun).

https://doi.org/10.1016/j.jallcom.2024.174693
Received 17 February 2024; Received in revised form 4 April 2024; Accepted 28 April 2024

severely limited the evolution of H_2, and hindered the production of syngas. Besides, their weak affinity for target H^+ and CO_2 molecules leads to a low total catalytic reaction rate [13–17]. In comparison, Co nanoparticles show high H_2 evolution activity and promising total catalytic reaction rate, but the poor selectivity for CO_2 impeded their application in producing syngas.

Constructing metal alloyed composites have proven to be effective in modifying the electronic structure, which optimized the adsorption energy of target H^+ and CO_2 [18–20]. Therefore, building copper-cobalt alloy system, in which electronic structure transformation may improve the selectively for CO_2 and provide opportunities for producing syngas [21,22]. Based on the Cu-Co alloy system, it is possible to regulate CO_2 electrocatalytic reaction rate for achieving target proportion of CO and H_2 ($CO:H_2$=1:1, 1:2, and 1:3) by optimizing the electronic structure of the Cu-Co alloy electrocatalyst.

Nevertheless, Co-Cu alloy is thermodynamically metastable and magnetically complex, which makes the material preparation and the associated theoretical calculations considerably challenging. In the previous researches, the Co-Cu alloy was explicitly prepared through a complex method, in which the sandwich-shaped Co-Cu composite was acquired by vapor deposition and subsequently prepared into Co-Cu alloy with laser ablation [23]. In this study, we developed a novel strategy to uniformly integrate substantial Cu^{2+} ions within a ZIF-67 MOF framework, which was converted into Co-Cu alloy nanoparticles embedded within carbon nanospheres via calcination in nitrogen atmosphere. The formation of the Co-Cu alloy has been confirmed by systematical characterization, including SEM, TEM, EDS and Raman spectroscopy. The best Co-Cu composite catalyst was the Co_1Cu_3@C sample, which indicated a total catalytic current of 29.8 mA·cm^{-2} at −0.7 V vs RHE. Both experimental methods and DFT calculation method have been used for exploring the influence of the Co-Cu alloy component on the catalytic performance enhancement.

2. Experiment

2.1. Material

2-Methylimidazole, triethylamine, and Nafion were from Adamas-beta, Shanghai Taitan Technology Co. Anhydrous cobalt (II) nitrate ($Co(NO_3)_2$), and anhydrous copper(II) nitrate ($Cu(NO_3)_2$) were acquired from Sigma-Aldrich. Methanol was purchased from Greagent, Shanghai Taitan Technology Co. Reagents and solvents were of analytical reagent (AR) grade and were used without further purification.

2.2. Preparation of MOFs

ZIF-67 was firstly prepared according to a facile process reported previously [21]. 4.45 mmol anhydrous cobalt nitrate and 39.5 mmol 2-methylimidazole were firstly dissolved in 15 ml methanol separately and then mixed slowly. After adding 0.75 ml triethylamine, the mixture was stirred for 24 h to ensure completely reaction. The resulting sample was washed with methanol and ethanol for three times each, and then dried at 80 °C to obtain ZIF-67.

Bimetallic MOF was synthesized by a similar procedure (Scheme 1). Anhydrous cobalt nitrate was firstly mixed with 0.75 ml triethylamine in 15 ml methanol to form Solution A. Anhydrous copper nitrate and 39.5 mmol 2-methylimidazole were dissolved in 15 ml methanol to form Solution B. After slowly adding Solution A into solution B, the mixture was stirred for 24 h. The sample was washed with methanol and ethanol and dried at 80 °C to obtain bimetallic MOFs. The total amount of cobalt and copper ions was set as 4.45 mmol and the molar ratio between Co^{2+}/Cu^{2+} was 1:0, 8:1, 3:1, 1:1, 1:3, 1:8 and 0:1 (noted as Co-MOF, Co_8Cu_1-MOF, Co_3Cu_1-MOF, Co_1Cu_1-MOF, Co_1Cu_3-MOF, Co_1Cu_8-MOF, and Cu-MOF, respectively.).

2.3. Preparation of bimetallic MOFs derivatives

In order to acquire bimetallic MOF derivatives electrocatalysts, the MOF samples obtained above were calcined at 750 °C for 2 h under a nitrogen atmosphere. The prepared samples were named as Co@C, Co_8Cu_1@C, Co_3Cu_1@C, Co_1Cu_1@C, Co_1Cu_3@C, Co_1Cu_8@C, and Cu@C, respectively. In order to obtain the best fabrication parameter, the Co_1Cu_3-MOF were also calcinated at 550 °C and 950 °C under the same atmosphere (noted as Co_1Cu_3@C-550 and Co_1Cu_3@C-950) and compared with the sample obtained at 750 °C.

2.4. Preparation of catalytic electrode

All samples obtained above were mixed with absolute ethanol and grounded for 30 min. After drying in air, the powders were collected for the preparation of electrodes,

To prepare the catalyst inks, 10 mg catalyst, 900 μl isopropanol, 40 μl ultrapure water, and 60 μl 5 % Nafion were mixed in specimen vials. The mixtures were ultrasonically dispersed for 30 min. Finally, 20 μl ink was coated on a glassy carbon electrode through drip coating and the loading amount was 1 mg·cm^{-2}.

2.5. Electrocatalytic performance

The electrocatalytic reduction of CO_2 was conducted in H-cell reactor with an electrolyte solution of 0.5 M $KHCO_3$. Before the reaction, high-purity CO_2 was introduced into the electrolyte for 30 min to ensure the solution was completely saturated with CO_2. All the gaseous products were detected by Agilent GC 7890B. Electrochemical properties of the samples were characterized by an electrochemical workstation CHI660d.

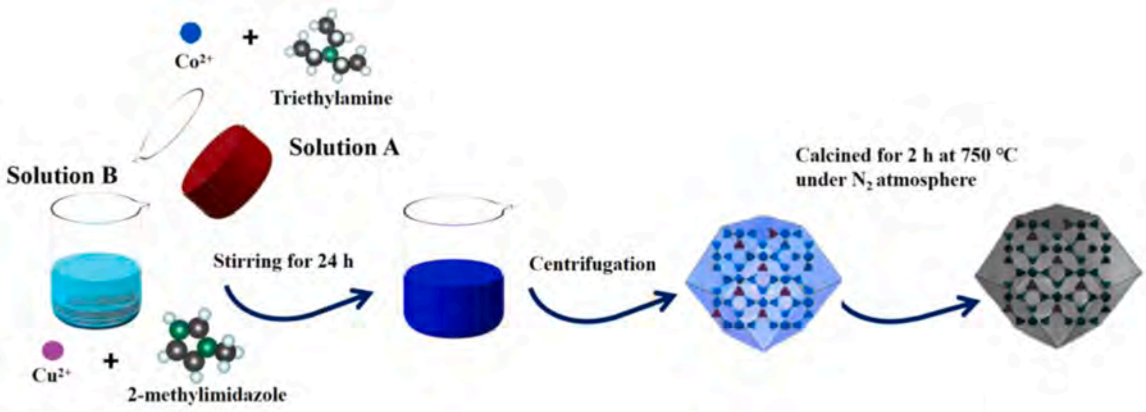

Scheme 1. Preparation of bimetallic MOFs and bimetallic MOFs derivatives.

2.6. DFT models and calculations

All DFT calculations were performed using the Vienna Ab initio Simulation Package (VASP) [24]. PBE was used to describe the exchange correlation energy and DFT-D3 was applied for dispersion correction [25,26]. In calculations, encut energy was set 550 eV. The convergence criteria were set at 10^{-5} eV. For all systems, spin polarization was employed and the vacuum layer was set to 15 Å.

In differential charge density calculations, the initial models of the calculation were based on a model with sufficient structural optimization. The convergence criterion of the self-consistent field (SCF) calculations for calculate electron density, were set to 1×10^{-8} eV. FFT grid mesh density was set to $150\times150\times150$. In the presented schemes, dark blue represents copper, while dark red denoted cobalt. Moreover, light blue indicated the gain of electrons, whereas yellow signified a loss of electrons.

In the projected density of states calculation, the cut-off energy was set at 750 eV. The convergence criterion of the Self-consistent field (SCF) calculations, were set to 1×10^{-8} eV. The KPOINT was set as $8\times8\times8$ for the better accuracy of density of states calculations.

The surface models were constructed with 96 metal atoms, which had translational repeatability in the horizontal direction. The cluster models consisted of 50 metal atoms, and their translational repeatability were interrupted with a 5 Å vacuum layer. In surface models and cluster models, the bottom two layers of atoms were fixed in order for a reasonable structure. In the adsorption energy calculation, the Co-Cu alloy models were constructed with top layer of Co and Cu, separately. It was recognized that *COOH is an essential intermediate product for the electrocatalysis of CO_2 to CO. Therefore, we carried out a series of calculations on $*CO_2$, *COOH and *CO. Addtionally, the various small molecules in the adsorption energy were also corrected reasonably.

3. Discussion

The micromorphology and composition of Co, Cu and bimetallic MOFs as precursors for CoCu@C electrodes were firstly analyzed. XRD results confirmed the successful preparation of both Co-MOF and Co_1Cu_3-MOF. As given by Fig. 1a, the XRD diffraction patterns of the as-synthesized Co-MOF (ZIF-67) matched well with the literature data [21]. Bimetallic MOFs also exhibited similar XRD patterns with ZIF-67, indicating a similar crystal structure. SEM has revealed that the as-prepared Co-MOF exhibited a nano-polyhedral surface topography, which was in consistency with previous results [21]. Furthermore, as observed in SEM images, Co_1Cu_3-MOF demonstrated excellent crystallinity and maintained a typical polyhedral morphology of ZIF-67 (Fig. 1b-c), indicating that the addition of Cu^{2+} ions does not influence the lattice structure of ZIF-67. As given by the EDS mapping and line-scan results in (Fig. 1e-i), Co^{2+} and Cu^{2+} ions were both evenly dispersed in Cu_1Co_3-MOF particles. The actual proportion of Co and Cu elements were measured as 68 % and 32 %, respectively. Combined with the following evidences: 1. Co-MOF and Co_1Cu_3-MOF exhibited the same crystal structure, and XRD results exhibited no impurities present in the Co_1Cu_3-MOF. 2. The large amounts of Cu^{2+} ions were introduced into the Co_1Cu_3-MOF and the Cu^{2+} ions were evenly dispersed. It could be indicated that the Cu^{2+} ions replace some sites of the Co^{2+}, engaging in the coordination reaction. Notably, by tradition method, it is difficult to explicitly introduce 5 % or more Cu element into Co sites in ZIF-67 [27]. In this work, it was found that Cu^{2+} ions can not react with 2-methylimidazole to form the MOF without triethylamine by the method of Co-MOF (ZIF-67) preparation, which indicated that Cu^{2+} ions exhibited weaker reactivity than Co^{2+} ions. In order to force the weaker Cu^{2+} ions engaging in the reaction, Cu^{2+} ions and 2-methylimidazole were mixed in advance to form the Cu^{2+} complex ions. The Co^{2+} and triethylamine were added to react with the Cu^{2+} complex ions, forming the uniform Co-Cu bimetallic MOFs.

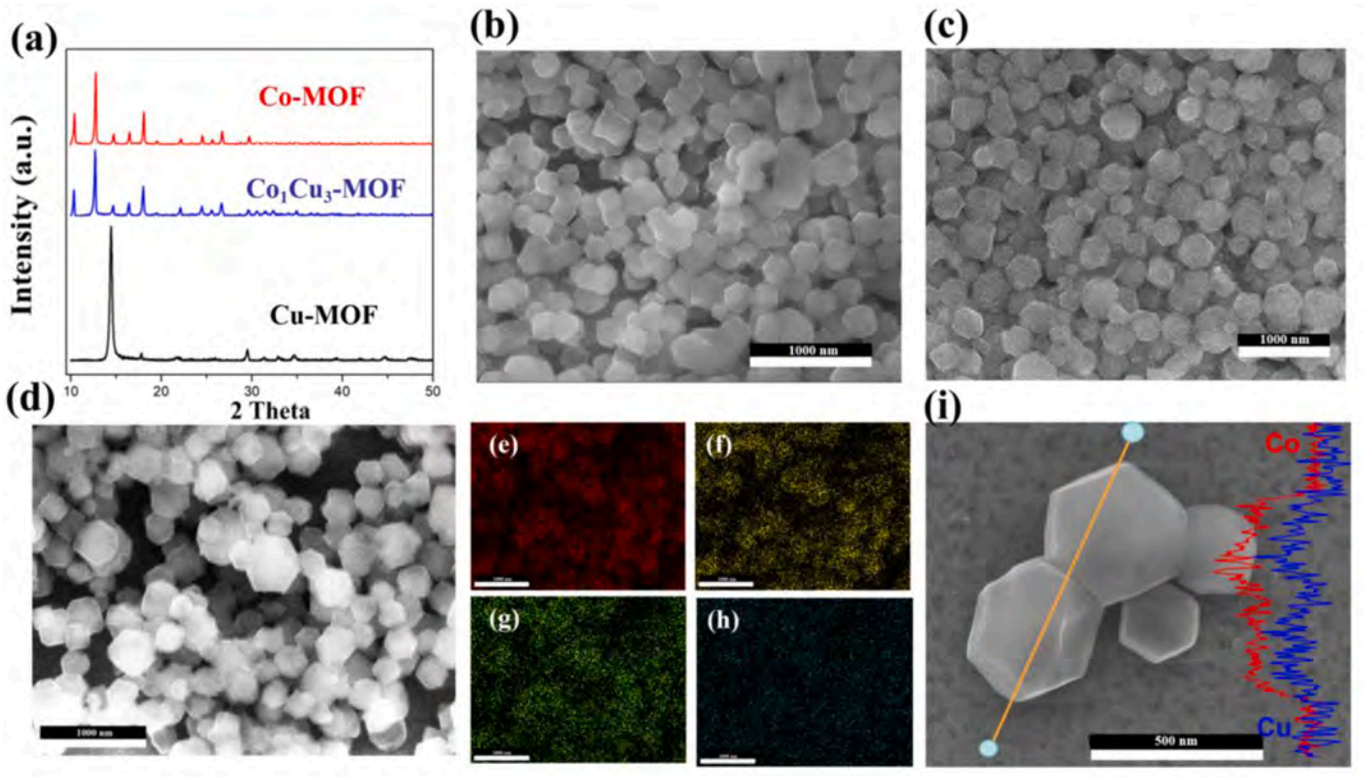

Fig. 1. (a) X-ray diffraction (XRD) patterns of Co-MOF (ZIF-67), Cu-MOF and Co_1Cu_3-MOF. (b) Scanning electron microscope (SEM) image of Co-mof. (c, d) Scanning electron microscope (SEM) images of Co_1Cu_3-MOF. Energy dispersive x-ray (EDX) mapping images of (e) **C**, (f) **N**, (g) **Co**, and (h) **Cu** in Co_1Cu_3-MOF. (i) Energy dispersive x-ray (EDX) line-scan image of Co_1Cu_3-MOF.

After 2 h calcination, the synthesized CoCu@C nanoparticles showed a spherical shape with sizes similar to that of the original MOFs. (Fig. 2a). Both fcc (face-centered cubic) elemental Co and fcc elemental Cu were observed in the XRD pattern of CoCu@C (Fig. 2b). The diffractions peaks of Co(111), Co (200) and Co(220) were located at 44.22°, 51.52° and 75.85°. The diffractions peaks of Cu(111), Cu (200) and Cu(220) were located at 43.34°, 50.48° and 74.17°.

Electrocatalytic performance tests on the 750 °C calcinated catalyst samples (Fig. 3a, Fig. 3g) were performed. For comparison, the concentration of all the products detected from the GC were converted to catalytic current density in the method described in the supplementary information. *The GC results demonstrated that the gaseous carbon-containing products were comprised solely of carbon monoxide (Fig. S8). The ^{1}H NMR results indicated the absence of liquid-phase products (Fig. S9).* At −0.8 V vs RHE, the total reduction current density of Cu@C and Co@C were 5.98 mA·cm^{-2} and 17.59 mA·cm^{-2}, respectively. Co@C indicated a better performance in total reduction current density. This trend becomed more pronounced at −0.4 V vs RHE, where the current density of Cu@C and Co@C were 0.278 mA·cm^{-2} and 3.09 mA·cm^{-2}, respectively.

As the contents of Cu increases, the catalytic performance of the samples first increased and then decreased, with Co_1Cu_3@C exhibiting the highest total reduction current of mA·cm^{-2} at −0.7 V vs RHE, which is 2.56 times that of Co@C (11.7 mA·cm^{-2}) (Figs. 3a-3h). The CO electrocatalytic current density improved from 3.5 mA·cm^{-2} (Co@C) to 11.67 mA·cm^{-2} (Co_1Cu_3@C) at −0.7 V vs RHE, compared with the Co@C sample. The CO Faraday efficiency has also been improved from 28 % to 34 % (-0.7 V vs RHE), compared with the Co@C. In the meantime, Co_1Cu_3@C exhibit a relatively large adjustable range of syngas ratios and CO Faraday efficiency. The CO selectivity (CO / CO+H_2) at different voltages from −0.4 V toward −0.7 V covers the ratio from 21 % to 37 % (Fig. 3i), whose CO:H_2 ratio covers about 1:1.7–1:4. The CO Faraday efficiency of Co_1Cu_3@C ranges from 21 % to 34 %. Notably, the same trend of CO selectivity and Faraday efficiency indicated that there were almost no by-products produced. Besides, the total Faraday efficiency of Co_1Cu_3@C for syngas is over 95 % from −0.4 V toward −0.7 V, further confirming the purity of the reduction products.

Subsequently, the differences in syngas generated by various Co-Cu composite were systematically discussed. For all examined catalysts, the proportion of CO within the produced syngas attained its maximum at an applied potential of −0.7 V vs RHE (Figs. 3a - 3i). With the higher applied voltage, there was a significant increase in the H_2 evolution rate, resulting in a correspondingly lower selectivity for CO. At lower voltage, a significant decrement in the CO generation rate was observed, resulting in a lower selectivity for CO. Consequently, we evaluated the syngas composition ratios produced by all the catalysts at a potential of −0.7 V vs RHE (Fig. S10). Among the catalysts tested, Co_1Cu_8@C exhibited the highest selectivity for CO, with the proportion of CO in the syngas reaching 36.3 %. As the concentration of copper increased, there was a significant reduction in the CO fraction of the syngas. Notably, in the case of the Cu@C catalyst, the CO concentration in the syngas composition experienced a significant decline, falling to 13.4 %. Compared to the Co_1Cu_8@C catalyst, those catalysts with higher cobalt contents exhibited decreased proportion of CO in the syngas produced. In the case of the Co@C catalyst, it was noted that the CO fraction decreased to 28.2 %. The analysis presented illustrated that Co_1Cu_8@C not only demonstrated the highest rate of CO production but also provided the highest CO selectivity.

Additionally, we tested materials with more various Cu/Co ratios, including Co_1Cu_6@C, Co_1Cu_5@C, Co_1Cu_4@C, Co_1Cu_3@C and Co_1Cu_2@C. The samples exhibited similar regularity in performance improvements. And Co_1Cu_3@C consistently demonstrated superior electrocatalytic performance (Fig. 4b).

After determining the optimal Cu/Co ratio, the influences of calcination temperature on the electrocatalytic performance were systematically investigated. Firstly, Co_1Cu_3@C samples were prepared with various calcination temperatures including 550 °C, 750 °C and 950 °C to induce different carbonization degree and the samples were named as Co_1Cu_3@C-550, Co_1Cu_3@C and Co_1Cu_3@C-950, respectively. Co_1Cu_3@C exhibited best total reduction current density and CO current density (Fig. 5a), while Co_1Cu_3@C-950 had weaker performance, and Co_1Cu_3@C-550 exhibited negligible catalytic properties.

Raman spectra were analyzed to characterize carbonization degree of the samples. The peak of Co_1Cu_3@C-550 at 684 cm^{-1} was associated to Co-MOF (ZIF-67), including the characteristic signals of Co-N and 2-methylimidazolate [28], which exhibited the low carbonization degree of Co_1Cu_3@C-550. In the Raman spectra of Co_1Cu_3@C and Co_1Cu_3@C-950, the peak near 684 cm^{-1} vanished, indicating that the carbon framework can form stably at 750 °C or above (Fig. 5b). The degree of carbonization was closely related to material performance for carbon skeleton could provided migration channels for electrons, and thus superior electrocatalytic performance. In contrast, Co_1Cu_3@C-550 presented negligible carbonization and thus poor electron conductivity, which was in accordance with its lame catalytic performance. In addition, we attempted to extract the metal particles in the 750 °C calcined sample. The experimental results showed that the remaining carbon frame did not exhibit notable catalytic performance (Fig. S11). The

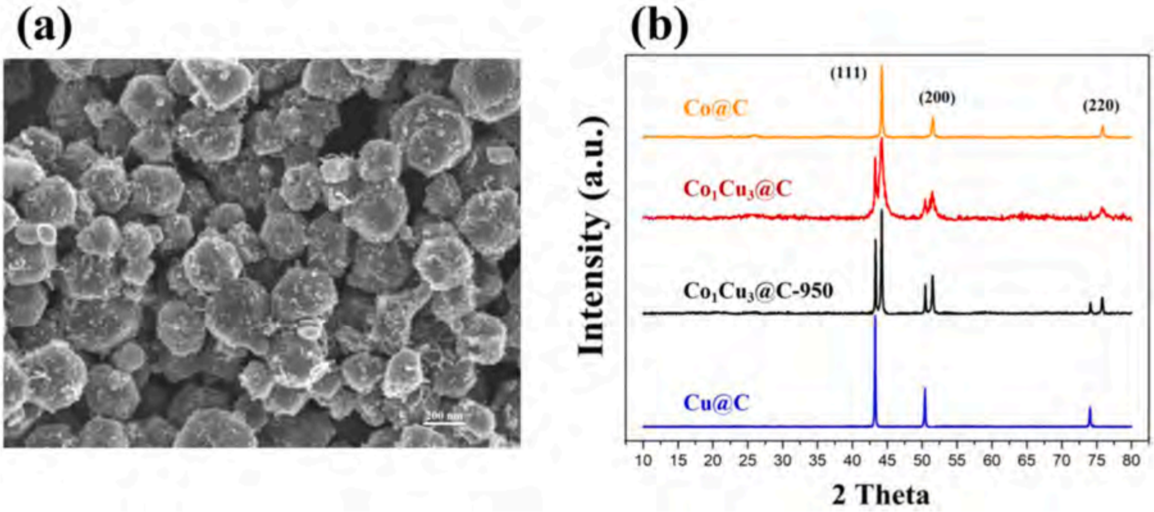

Fig. 2. (a) Scanning electron microscope (SEM) image of Co_3Cu_1@C. (b) X-ray diffraction (XRD) patterns of Co@C, Cu@C, Co_3Cu_1@C, and Co_3Cu_1@C-950.

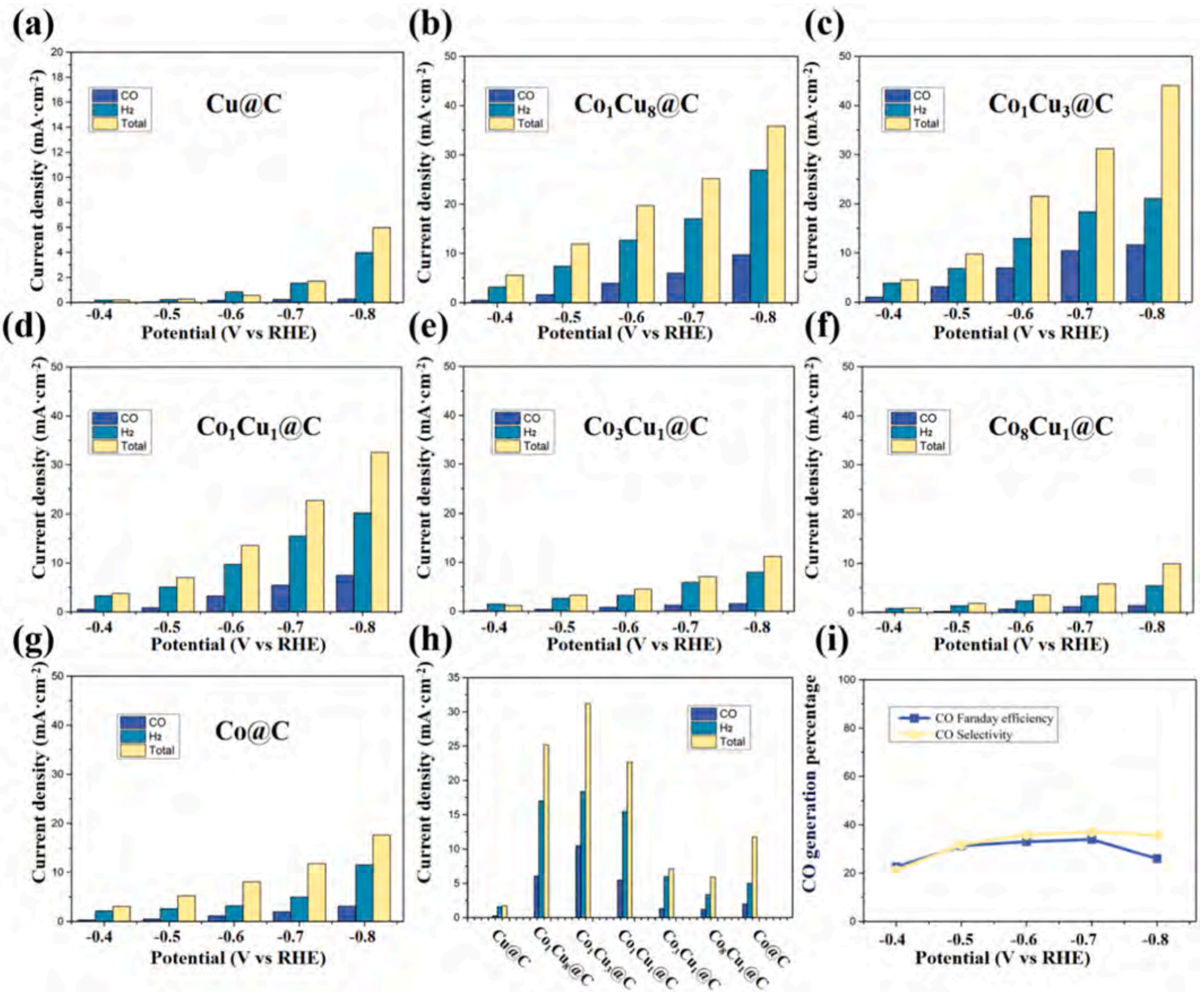

Fig. 3. (a) Catalytic reduction current density of Cu@C, (b) Co_1Cu_8@C, (c) Co_1Cu_3@C, (d) Co_1Cu_1@C, (e) Co_3Cu_1@C, (f) Co_8Cu_1@C, (g) Co@C. (h) Electrocatalytic reduction current density of different catalysts at −0.7 V vs RHE. (i) CO selectivity (CO / CO+H_2) and Faraday efficiency at different voltages.

result indicated that metal nanoparticles played a dominant role in the synergistic effects.

For an in-depth examination of the carbonization products, TEM characterization was conducted. As given by Fig. 6c, in the 750 °C samples, metal nanoparticles in the size range of 5–10 nm (Fig. 5c) were uniformly dispersed in a carbon matrix. Three different crystalline interplanar spacings (2.087 Å, 2.056 Å, 2.040 Å) were measured within the high resolution TEM (HRTEM) image of a single nanoparticle, corresponding to Cu, Co-Cu alloy, and Cu, respectively (Fig. 5d) [29,30]. This result confirmed the formation of Co-Cu alloy in the Co_1Cu_3@C sample. When the calcination temperature increased to 950 °C, fusion of metal nanoparticles occurred and larger particles within 100–300 nm range emerged (Fig. 5e). As given by the HRTEM results in Figs. 5f and 5g, the crystalline interplanar spacing of large metal nanoparticles (~100 nm) was measured as 2.086 Å, matching well with the Cu (111) face, while the crystalline interplanar spacing of small nanoparticles (5–10 nm), which was calculated as 2.035 Å, could be assigned to Co (111) facet. Changes in the micromorphology and sizes of the metal nanoparticles indicated the fusion and re-crystallization of Cu with lower melting point at 950 °C.

Similar results could be observed in the XRD analysis (Fig. 5h). In addition to the diffraction peaks assigned to Cu and Co crystals, small shoulder peaks situated between them were also observed in Co_1Cu_3@C, which was attributed to the formation of Co-Cu metastable alloy. The Co-Cu was considered to be a solid solution consist of Cu and Co, retaining an fcc crystal structure with a lattice parameter (a=3.58 Å) between 3.613 Å of fcc Cu and 3.545 Å of fcc Co. On the contrary, Co_1Cu_3@C-950 only exhibited sharp and smooth peaks for Cu and Co crystals, further confirmed the destruction of Co-Cu nanoalloys.

In conjunction with the results, it could be inferred that in the Co_1Cu_3@C-950 sample, Co and Cu significantly separated and most of the alloy phase was disrupted, resulting in a substantial drop in performance. Therefore, it could be confirmed that the alloy phase played a pivotal role in enhancing catalytic performance within this system.

Furthermore, DFT calculations was conducted to further elucidate the mechanism behind the enhancement in catalytic performance. Previous research has indicated that metal solid solutions tend to stack in layers [23,31]. Four potential lattice structures of metal solid solutions were devised, among which the structure shown in the Fig. 7a was found to be the closest match to the actual XRD pattern (Fig. S13-S14).

The DOS (density of state) calculations about Cu system, Co-Cu alloy system and Co system (Figs. 6a-6c, Fig. S15) were conducted. At the Fermi surface (0 eV), all the density of state images were continuous and non-zero, which indicated the metallicity of all systems (Figs. 6d-6i). In

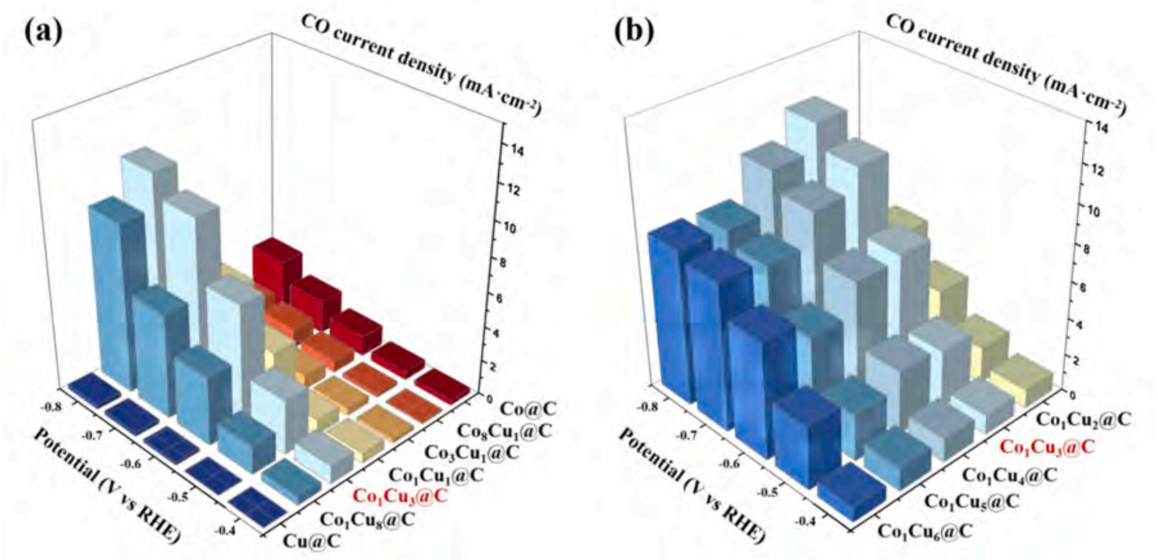

Fig. 4. (a) CO catalytic reduction current density of Cu@C, Co_1Cu_8@C, Co_1Cu_3@C, Co_1Cu_1@C, Co_3Cu_1@C, Co_8Cu_1@C and Cu@C. (b) CO catalytic reduction current density of Co_1Cu_6@C, Co_1Cu_5@C, Co_1Cu_4@C, Co_1Cu_3@C and Co_1Cu_2@C.

elemental Cu, unpaired electrons had almost no effect on the system, showing typical characteristics of non-magnetic systems (Fig. 6d). In elemental Co, there were a large number of unpaired d-orbital electrons, the spin of which leaded to band polarization, making elemental Co a typical magnetic system (Fig. 6f).

The d-band center theory holds that the center of the d-band projected state density can qualitatively judge the adsorption capacity of the catalyst towards target small molecules, and can be used to explain the catalytic performance [32]. In adsorption process, the half d-bond with higher energy has higher contribution. The spin-down d-band center of Cu system, Co system and Co (Co-Cu system), were identified as −2.94 eV, 0.12 eV and 0.02 eV respectively. The d-band center of Co was significantly higher than that of Cu, which indicated stronger adsorption capacity and the higher total catalytic reduction current.

The shift of the PDOS of Cu indicated the electron transferred between the Co and Cu (Fig. 6d-e). In the differential charge density images, a migration of electrons from Co to Cu (Fig. 7a-d) could be observed in the Co-Cu composite, which could be attributed to the lower DOS energy of the Cu (Fig. 7h).

In this work, DFT+U method was employed for adsorption energy calculation finally with systemically tests. According to the HRTEM results above, 6 layers (111) faces were set as the exposed surface of the material during constructing the surface models. Because of the magnetism produced by unpaired electrons, electronic step calculations (SCF) did not reach convergence results without DFT+U method, which leaded to unreasonable calculation results (Fig. S16). Subsequently, DFT+U method was employed to deal with the adsorption models, which corrected the inter-electron Coulomb interactions. All the adsorption energy calculations rapidly reached the convergence results. However, the adsorption energy results still exhibited obvious thermodynamic errors (Table S4), which might be attributed to complex magnetic conditions in periodic systems.

After selecting DFT+U method to research the system, it has been found that the cluster models were more reasonable rather than the surface models. For one thing, the periodic magnetism has little effect on adsorption energy. For another, the nanoparticles in the material were far away from periodic macroscopic systems. Therefore, cluster models with a diameter of about 1 nm were constructed and analyzed with DFT+U method to precisely describe the adsorption behavior of CO_2 and its reduction intermediates. The adsorption energy calculations ended with convergence and reasonable results. Based on the above data, we plotted the reaction pathway (Fig. 8a).

In the electrocatalytic reduction process, the adsorbed CO_2 molecule acquires the first electron, resulting in its conversion to *CO_2^-. This structure subsequently captures H^+ from the aqueous solution, leading to the formation of *CO_2H. It is widely acknowledged that variations in the adsorption structure of *CO_2H dictated the divergences observed in the reaction mechanism [33,34]. The main divergence in the reaction mechanism arised from whether *CO_2H existed in the form of *COOH or *OCHO. In the DFT computations of the adsorption energy, we observed a substantial adsorptive interaction between the carbon atom of the *CO_2H and the metal sites on the catalyst surface, facilitating the transformation of *CO_2H into *COOH. DFT calculation results indicated a weak interaction between the catalyst surface and the oxygen atom in *CO_2H, implying that the transformation of *CO_2H into *OCHO was not facilitated. In the present investigation, the formation of *COOH was found to be more favorable. After receiving the secondary electron, the *COOH proceeded to release a water molecule, culminating in the formation of *CO. The dissociative adsorption of the *CO results in the release of CO, thus facilitating CO_2 to CO.

Within the reaction pathway, the Co atoms extracted from Co-Cu exhibited more significant electrochemical activity compared to other surfaces (Fig. 8a). Concretely, that surface exhibited deeper energy drops in the two electrochemical steps of *COOH formation and *CO formation, which means that the Gibbs free energy of the reaction on Co-Cu is more negative. Electrochemical reduction reactions proceed more spontaneously on the surface of Co-Cu. It is generally accepted that the step of CO removal involves the spontaneous increase in entropy and the adsorption of solvents, which ultimately leads to a smooth reaction [12,20]. The presence of electron migration from elemental Co to Cu in Co-Cu alloy was found as the dominant reason for the deep energy drops on Co atoms, which further resulted in the significantly enhanced electrocatalytic activity of Co_1Cu_3@C system towards CO_2 reduction.

4. Conclusion

CoCu@C composite catalysts with improved performance in the electrocatalytic reduction of CO_2 was fabricated by simply carbonizing CuCo-bimetallic MOFs. The formation of Co-Cu alloys promoted the migration of electrons and therefore significantly improved the total reduction current compared to single Co@C. In addition, a relatively large adjustable range of syngas ratios and CO Faraday efficiency were

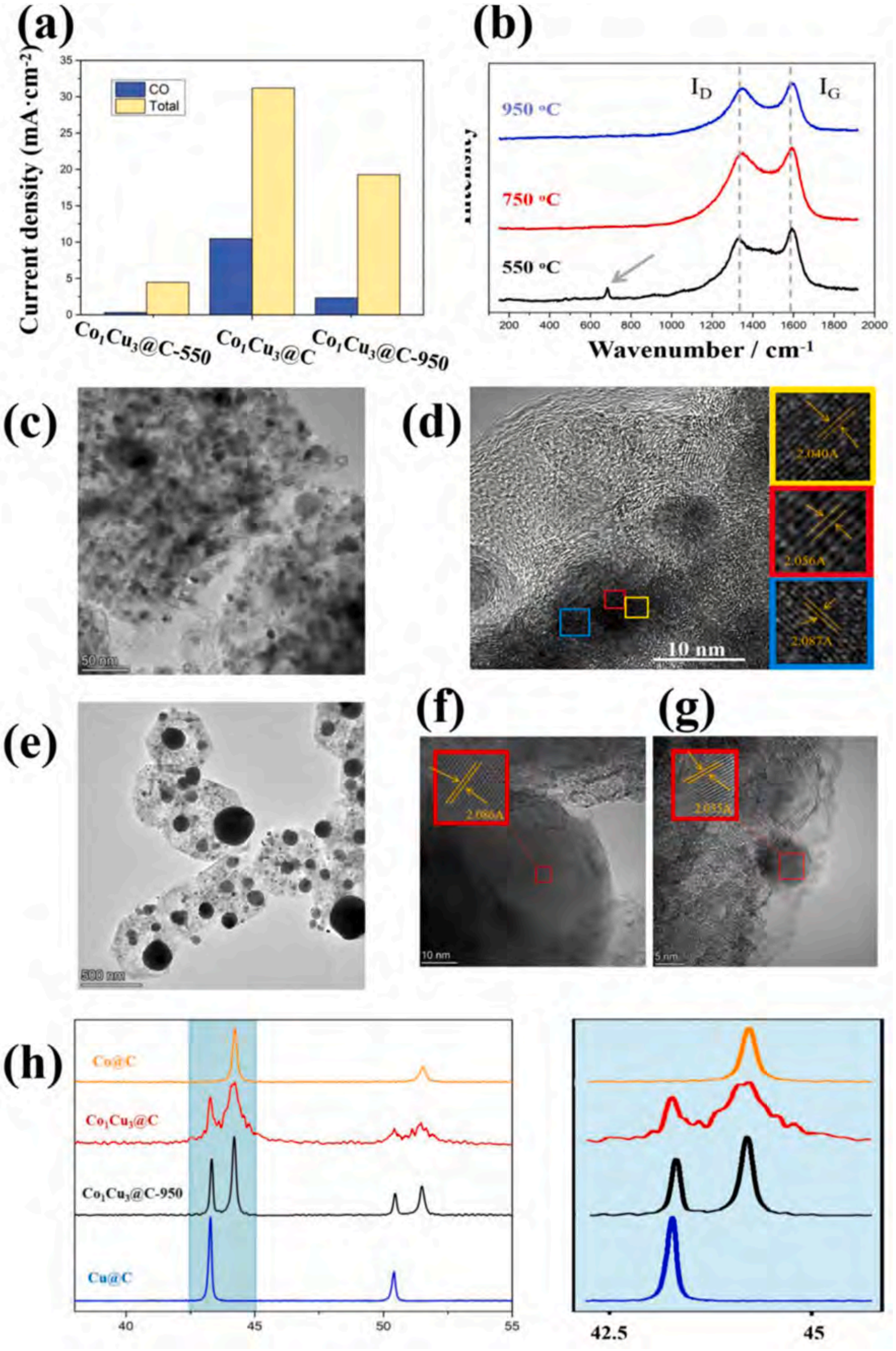

Fig. 5. (a) Electrocatalytic reduction current density of Co_1Cu_3@C-550, Co_1Cu_3@C and Co_1Cu_3@C-950 at −0.7 V vs RHE. (b) Raman spectroscopy image of Co_1Cu_3@C-550, Co_1Cu_3@C and Co_1Cu_3@C-950. (c) Transmission electron microscope (TEM) image of Co_1Cu_3@C. (d) High-resolution transmission electron microscope (HR-TEM) image of Co_1Cu_3@C. (e) TEM image of Co_1Cu_3@C-950. (f), (g) HR-TEM image of larger particles in Co1Cu3C-950. (h) Enlarged XRD pictures of Co@C, Co_1Cu_3@C, Co_1Cu_3@C-950, and Cu@C.

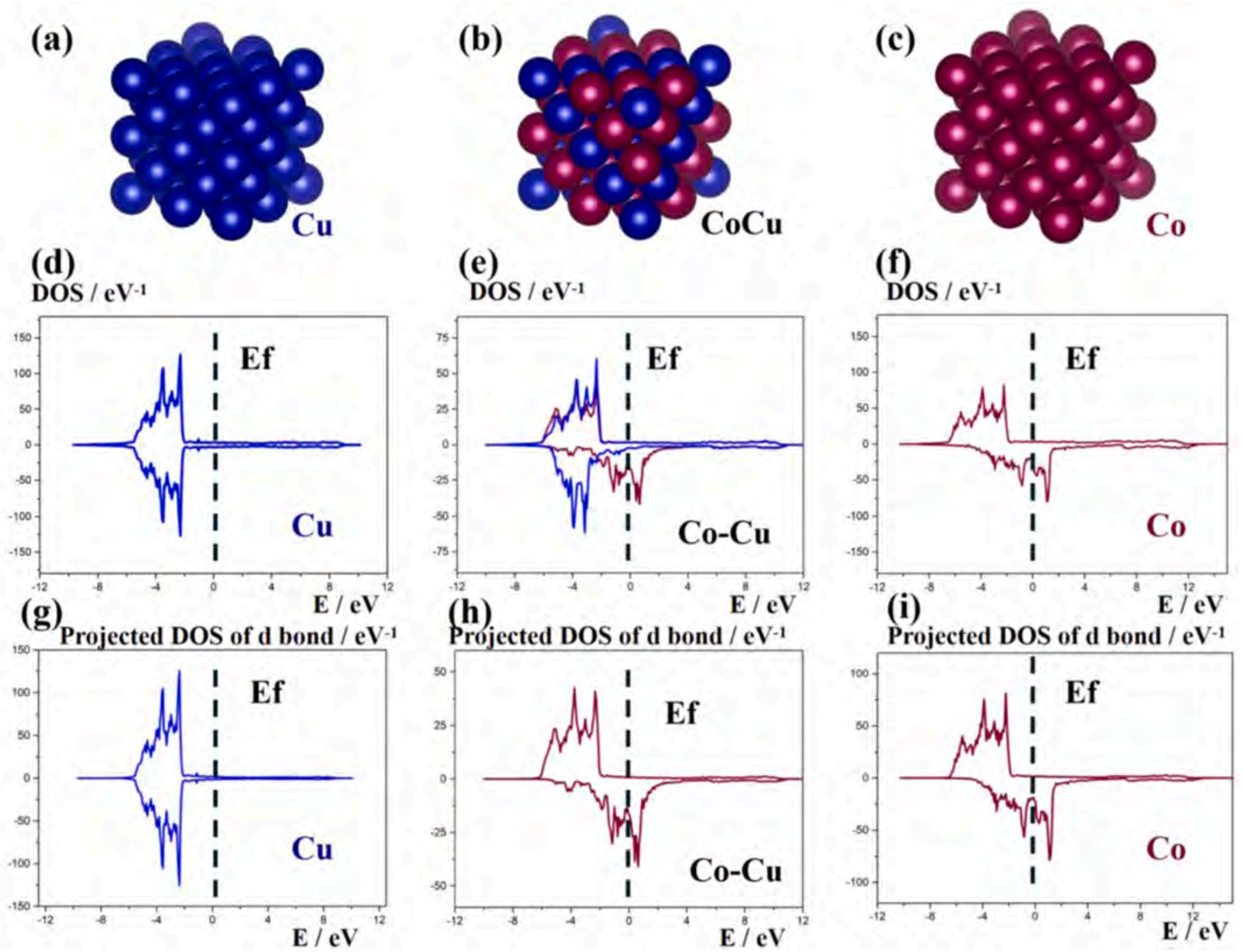

Fig. 6. (a) Fcc Cu with a 2×2x2 supercell. (b) Fcc Co-Cu stratified according to (111) crystal faces. (c) Fcc Co with a 2×2x2 supercell. (d) Density of state(DOS) of Fcc Cu. (e) DOS of Fcc Co-Cu. (f) DOS of Fcc Co. (g) Projected density of state(PDOS) of Cu d-bond in fcc Cu. (h) PDOS of Co d-bond in fcc Co-Cu. (i) PDOS of Co d-bond in fcc Co.

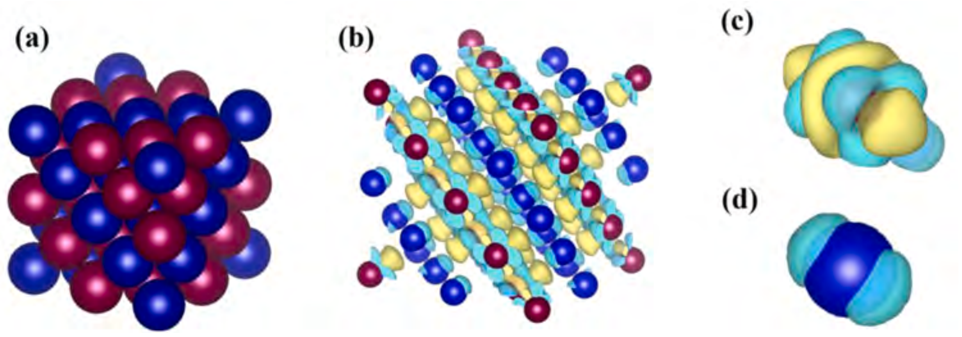

Fig. 7. (a) Fcc Cu with a 2×2x2 supercell. (b)Differential charge density image of Co-Cu. Light blue means electron rich zone and yellow means electron deficient zone. (c) Differential charge image of Co-Cu on Co atom. (d) Differential charge image of Co-Cu on Cu atom.

achieved, which meet well with the industrial needs. According to DFT analysis, the charge transferred from Co to Cu made Co atoms in Co-Cu alloy the best site for electrocatalytic reactions, which illustrated the relevance of the electron migration, adsorption energy and catalyst performance. This work provided a cost-effective electrocatalyst for syngas preparation and expanded understanding of Co-Cu alloy electrocatalytic systems.

CRediT authorship contribution statement

Gansheng Shi: Writing – review & editing, Methodology. **Yan Wang:** Writing – review & editing, Formal analysis. **Xiao Wang:** Writing – review & editing, Methodology. **Guanqing Song:** Writing – review & editing, Methodology. **Chi Song:** Writing – review & editing, Writing – original draft, Visualization, Methodology, Investigation, Formal

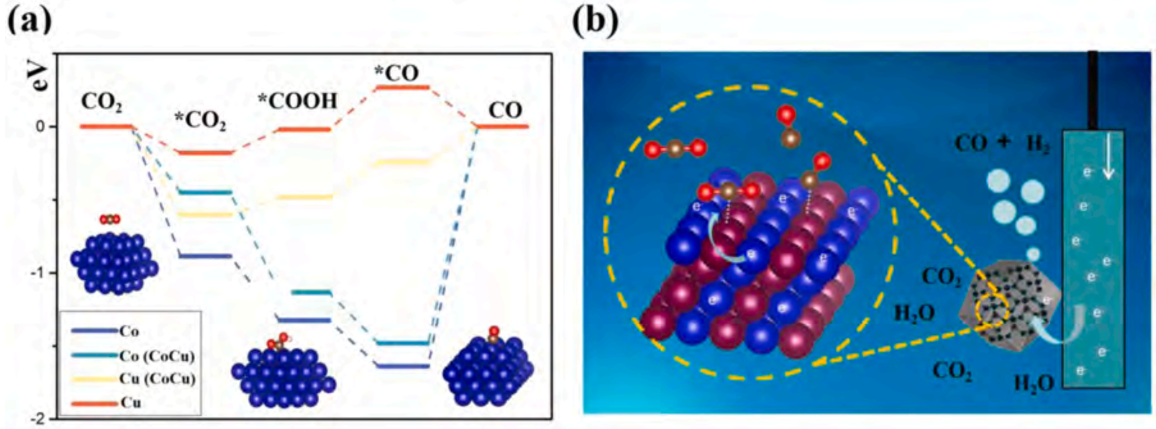

Fig. 8. (a) Free energy diagrams for CO_2 reduction to CO on Co, Cu, Co(CoCu), Cu(CoCu). (b) A schematic view of the CO_2 reduction to CO on the bimetallic MOFs derivatives.

analysis, Data curation, Conceptualization. **Jing Sun:** Writing – review & editing, Resources, Project administration. **Jiajun Yu:** Methodology. **Xiaofeng Xie:** Resources, Project administration.

Declaration of Competing Interest

The authors declare that they have no known competing financial interests or personal relationships that could have appeared to influence the work reported in this paper.

Data Availability

Data will be made available on request.

Acknowledgements

This study was financially supported by the National Natural Science Foundation of China (52072387), the Key Collaborative Research Program of the Alliance of International Science Organization (ANSO-CR-KP-2020-13), the Natural Science Foundation of Shanghai (22ZR1471800).

Appendix A. Supporting information

Supplementary data associated with this article can be found in the online version at doi:10.1016/j.jallcom.2024.174693.

References

[1] D. Xu, K. Li, B. Jia, W. Sun, W. Zhang, X. Liu, T. Ma, Electrocatalytic CO_2 reduction towards industrial applications, Carbon Energy 5 (2022).
[2] S. Sung, D. Kumar, M. Gil-Sepulcre, M. Nippe, Electrocatalytic CO_2 reduction by imidazolium-functionalized molecular catalysts, J. Am. Chem. Soc. 139 (2017) 13993–13996.
[3] F. Yang, X. Ma, W.-B. Cai, P. Song, W. Xu, Nature of oxygen-containing groups on carbon for high-efficiency electrocatalytic CO_2 reduction reaction, J. Am. Chem. Soc. 141 (2019) 20451–20459.
[4] S. Jin, Z. Hao, K. Zhang, Z. Yan, J. Chen, Advances and challenges for the electrochemical reduction of CO_2 to CO: from fundamentals to industrialization, Angew. Chem. Int. Ed. 60 (2021) 20627–20648.
[5] B. Chang, Z. Min, N. Liu, N. Wang, M. Fan, J. Fan, J. Wang, Electrocatalytic CO_2 reduction to syngas, Green. Energy Environ. (2023).
[6] C. Li, Y. Wang, N. Xiao, H. Li, Y. Ji, Z. Guo, C. Liu, J. Qiu, Nitrogen-doped porous carbon from coal for high efficiency CO_2 electrocatalytic reduction, Carbon 151 (2019) 46–52.
[7] J. Sun, B. Yu, X. Yan, J. Wang, F. Tan, W. Yang, G. Cheng, Z. Zhang, High throughput preparation of Ag-Zn alloy thin films for the electrocatalytic reduction of CO_2 to CO, Materials 15 (2022).
[8] Z.-Z. Wu, F.-Y. Gao, M.-R. Gao, Regulating the oxidation state of nanomaterials for electrocatalytic CO_2 reduction, Energy Environ. Sci. 14 (2021) 1121–1139.
[9] S. Ringe, The importance of a charge transfer descriptor for screening potential CO_2 reduction electrocatalysts, Nat. Commun. 14 (2023).
[10] C. Guo, T. Zhang, X. Liang, X. Deng, W. Guo, Z. Wang, X. Lu, C.-M.L. Wu, Single transition metal atoms on nitrogen-doped carbon for CO_2 electrocatalytic reduction: CO production or further CO reduction, Appl. Surf. Sci. (533) (2020).
[11] Z. Tao, A.J. Pearce, J.M. Mayer, H. Wang, Bridge sites of Au surfaces are active for electrocatalytic CO_2 reduction, J. Am. Chem. Soc. 144 (2022) 8641–8648.
[12] D. Gao, H. Zhou, J. Wang, S. Miao, F. Yang, G. Wang, J. Wang, X. Bao, Size-dependent electrocatalytic reduction of CO_2 over Pd nanoparticles, J. Am. Chem. Soc. 137 (2015) 4288–4291.
[13] D. Wang, S. Dong, L. Wen, W. Yu, Z. He, Q. Guo, X. Lu, L. Wang, S. Song, J. Ma, Highly selective electrocatalytic reduction of CO_2 to HCOOH over an in situ derived hydrocerussite thin film on a Pb substrate, Chemosphere 291 (2022).
[14] W. Sun, Y. Liang, C. Wang, X. Feng, W. Zhou, B. Zhang, Computational design of copper doped indium for electrocatalytic reduction of CO_2 to formic acid, ChemCatChem 12 (2020) 5632–5636.
[15] H. Wu, Z. Li, Y. Liu, X. Zou, L. Yin, S. Lin, A cost-effective indium/carbon catalyst for highly efficient electrocatalytic reduction of CO_2 to HCOOH, Sustain. Energy Fuels 5 (2021) 5798–5803.
[16] Y. Shitrit, M. Duraiyarasu, J. Kumar, S. Reddy, A. Ya'akobovitz, Y.S. Cohen, E. Edri, Deposition of Bismuth nanoplatelets onto graphene foam for electrocatalytic CO_2 reduction, ACS Appl. Nano Mater. 5 (2022) 16354–16364.
[17] X. Wang, Y. Zou, Y. Zhang, B. Marchetti, Y. Liu, J. Yi, X.-D. Zhou, J. Zhang, Tin-based metal organic framework catalysts for high-efficiency electrocatalytic CO_2 conversion into formate, J. Colloid Interface Sci. 626 (2022) 836–847.
[18] J. He, N.J.J. Johnson, A. Huang, C.P. Berlinguette, Electrocatalytic alloys for CO_2 reduction, ChemSusChem 11 (2017) 48–57.
[19] J. He, K.E. Dettelbach, D.A. Salvatore, T. Li, C.P. Berlinguette, High-throughput synthesis of mixed-metal electrocatalysts for CO_2 reduction, Angew. Chem. Int. Ed. 56 (2017) 6068–6072.
[20] J. Wang, G. Zhang, H. Liu, Z. Li, L. Wang, J. Tressel, S. Chen, High-performance electrocatalytic reduction of CO_2 to CO by ultrathin PdCu alloy nanosheets, Sep. Purif. Technol. 320 (2023).
[21] J.-X. Gu, X. Zhao, Y. Sun, J. Zhou, C.-Y. Sun, X.-L. Wang, Z.-H. Kang, Z.-M. Su, A photo-activated process cascaded electrocatalysis for the highly efficient CO_2 reduction over a core–shell ZIF-8@Co/C, J. Mater. Chem. A 8 (2020) 16616–16623.
[22] P. Hou, W. Song, X. Wang, Z. Hu, P. Kang, Well-defined single-atom cobalt catalyst for electrocatalytic flue gas CO_2 reduction, Small 16 (2020).
[23] P. Wu, E.Y. Jiang, H.L. Bai, H.Y. Wang, Evolution of microstructure in Co–Cu multilayers during thermal annealing, Phys. Status Solidi (A) 161 (1997) 389–397.
[24] G. Kresse, J. Furthmüller, Efficiency of ab-initio total energy calculations for metals and semiconductors using a plane-wave basis set, Comput. Mater. Sci. 6 (1996) 15–50.
[25] J.P. Perdew, K. Burke, M. Ernzerhof, Generalized gradient approximation made simple, Phys. Rev. Lett. 77 (1996) 3865–3868.
[26] S. Grimme, J. Antony, S. Ehrlich, H. Krieg, A consistent and accurateab initioparametrization of density functional dispersion correction (DFT-D) for the 94 elements H-Pu, J. Chem. Phys. 132 (2010).
[27] J.H. Cho, C. Lee, S.H. Hong, H.Y. Jang, S. Back, Mg Seo, M. Lee, H.K. Min, Y. Choi, Y.J. Jang, S.H. Ahn, H.W. Jang, S.Y. Kim, Transition metal ion doping on ZIF-8 enhances the electrochemical CO_2 reduction reaction, Adv. Mater. 35 (2022).
[28] Y. Li, Z. Jin, T. Zhao, Performance of ZIF-67 - Derived fold polyhedrons for enhanced photocatalytic hydrogen evolution, Chem. Eng. J. 382 (2020).
[29] X. Ma, Y. Ma, A.M. Nolan, J. Bai, W. Xu, Y. Mo, H. Chen, Understanding the polymorphism of cobalt nanoparticles formed in electrodeposition—an in situ XRD study, ACS Mater. Lett. 5 (2023) 979–984.
[30] M. Bersani, K. Gupta, A.K. Mishra, R. Lanza, S.F.R. Taylor, H.-U. Islam, N. Hollingsworth, C. Hardacre, N.H. de Leeuw, J.A. Darr, Combined EXAFS, XRD,

DRIFTS, and DFT study of nano copper-based catalysts for CO_2 hydrogenation, ACS Catal. 6 (2016) 5823–5833.

[31] Ş. Ţălu, M. Bramowicz, S. Kulesza, A. Ghaderi, V. Dalouji, S. Solaymani, Z. Khalaj, Microstructure and micromorphology of Cu/Co nanoparticles: Surface texture analysis, Electron. Mater. Lett. 12 (2016) 580–588.

[32] Y. Zhou, Z. Zhou, R. Shen, R. Ma, Q. Liu, G. Cao, J. Wang, Correlating electrocatalytic oxygen reduction activity with d-band centers of metallic nanoparticles, Energy Storage Mater. 13 (2018) 189–198.

[33] S.D. Rihm, J. Akroyd, M. Kraft, Modelling a detailed kinetic mechanism for electrocatalytic reduction of CO_2, Proc. Combust. Inst. 39 (2023) 5647–5655.

[34] L. Zhang, Z.J. Zhao, J. Gong, Nanostructured materials for heterogeneous electrocatalytic CO_2 reduction and their related reaction mechanisms, Angew. Chem. Int. Ed. 56 (2017) 11326–11353.